Meccanica (2021) 56:2691–2706
https://doi.org/10.1007/s11012-021-01410-7

Dynamic load and thermal coupled analysis for the inter-shaft bearing in a dual-rotor system

Peng Gao · Lei Hou · Yushu Chen

Received: 7 March 2021 / Accepted: 9 July 2021 / Published online: 5 August 2021
© Springer Nature B.V. 2021

Abstract The inter-shaft bearings are important supporting parts between higher and lower pressure rotors in dual-rotor systems, it is essential to analyze their temperatures during operation. This paper concentrates on the effect of the dynamics of the system on the temperatures of bearings, namely, the dynamic load is coupled with thermal behaviours. The dynamic load of the inter-shaft bearing is obtained by solving the dynamic equations of the system numerically. The friction heat generations (FHGs) under the dynamic load are obtained by Palmgren's empirical formula, based on which, the unsteady-state heat balance equations under the dynamic load are proposed considering the viscosity-temperature relationship of the lubricant. The steady-state and unsteady-state temperatures analysis of the inter-shaft bearing are carried out afterwards. The results show that the temperature of the inter-shaft bearing and the total FHG increase sharply and form two peaks in the "resonance zone" of the dual-rotor system, and gradually increase in the "non-resonance zone" of the system. The steady-state temperature of lower rotation speed in the "resonance zone" may be much higher than that of higher rotation speed in the "non-resonance zone". The load FHG plays a leading role in the "resonance zone", while the viscosity FHG plays a leading role in the "non-resonance zone".

Keywords Dynamic load · Inter-shaft bearing · Dual-rotor · Friction heat generation · Heat transfer

P. Gao · L. Hou (✉) · Y. Chen
School of Astronautics, Harbin Institute of Technology, Harbin 150001, People's Republic of China
e-mail: houlei@hit.edu.cn

P. Gao
e-mail: gaopeng_hit@126.com

Nomenclature

M_t	Total friction torque
M_b	Load friction torque
M	Viscosity friction torque
Q_t	Total FHG
Q_b	Load FHG
Q	Viscosity FHG
Q_L	FHG taken by the lubricant
Q_r	FHG distributed to rollers
Q_i	FHG distributed to the inner ring
Q_o	FHG distributed to the outer ring
f_b	Factor depended on bearing type and load
f	Factor depended on bearing type and lubrication method
d_L	The inner diameter of the LP rotor
d	Nominal bore
d_i	Diameter of the inner ring
D_m	Pitch diameter
d_o	Diameter of the outer ring
D	Nominal outer diameter
d_H	The outside diameter of HP outer
d_r	Diameter of the roller
a_r	Length of the roller

B	Width of the bearing
m_{r}	Mass of rollers
m_{i}	Mass of the inner ring
m_{o}	Mass of the outer ring
m_{LP}	Mass of the part of LP rotor near the inner ring
m_{HP}	Mass of the part of HP rotor near the outer ring
h	Convective heat transfer coefficient
V	Line speed
V_{i}	Line speed of the inner ring
V_{o}	Line speed of the outer ring
k_{steel}	Thermal conductivity of steel
c_{steel}	Specific heat capacity of steel
α_{steel}	Thermal diffusivity of steel
T_{L}	The temperature of the lubricant
T_{r}	Temperature of rollers
T_{i}	The temperature of the inner ring
T_{o}	The temperature of the outer ring
T_{LP}	The temperature of the LP rotor part near the inner ring
T_{HP}	The temperature of the HP rotor part near the outer ring
T_{∞}	The temperature of the ambient
R_{ri}	Thermal resistance between rollers and the inner ring
R_{ro}	Thermal resistance between rollers and the outer ring
R_{Lr}	Thermal resistance between the lubricant and rollers
R_{Li}	Thermal resistance between the lubricant and the inner ring
R_{Lo}	Thermal resistance between the lubricant and the outer ring
R_{i}	Thermal resistance between the inner ring and the LP rotor
R_{o}	Thermal resistance between the outer ring and the HP rotor
R_{LP}	Thermal resistance between the LP rotor and the ambient
R_{HP}	Thermal resistance between the HP rotor and the ambient
x_1	Vertical displacement of the LP rotor
y_1	Horizontal displacement of the LP rotor
x_2	Vertical displacement of the HP rotor
y_2	Horizontal displacement of the HP rotor
θ_x	The rotational angle of the LP rotor around the x-axis
θ_y	The rotational angle of the LP rotor around the y-axis
φ_x	The rotational angle of the HP rotor around the x-axis
φ_y	The rotational angle of the HP rotor around the y-axis
x_{i}	Vertical displacement of the inner ring
y_{i}	Horizontal displacement of the inner ring
x_{o}	Vertical displacement of the outer ring
y_{o}	Horizontal displacement of the outer ring
m	Mass of rotor
J_{p}	Polar moment of inertia
J_{d}	Diameter moment of inertia
e	Unbalance of rotor
k	Stiffness coefficient of linear support
c	Damping coefficient of linear support
v	Kinematic viscosity of the lubricant
F_x	Inter-shaft bearing's force along the vertical direction
α	Thermal diffusivity
F_y	Inter-shaft bearing's force along the horizontal direction
A	Area
$\delta\blacksquare$	Virtual displacement
Nu	Nusselt number
θ_k	Angular position
Re	Reynolds number
δ_k	The relative deformation between the kth roller and rings
Pr	Prandtl number
$2\delta_0$	Radial clearance
Ta	Taylor number
l	Length of rotors
Bi	Biot number
r_{i}	The radius of the inner ring
Pe^*	Modified Peclet number
r_{o}	The radius of the outer ring
ω_1	LP rotor's rotation speed
n_{b}	Average pressed roller number
ω_2	HP rotor's rotation speed
N_{b}	Roller number
ω_{C}	Cage's rotation speed
K_{b}	Stiffness of the bearing
λ	Rotation speed ratio
F_{b}	Dynamic load

1 Introduction

The inter-shaft bearings [1] play a crucial role in dual-rotor systems of the high-speed rotating machine, including generator, aircraft engine and electric motor. The radial cylindrical roller bearings are usually used as the inter-shaft bearings to optimize the structure and reduce the vibration of the dual-rotor system. Different from other bearings only for support, both outer and inner rings are rotating with higher pressure (HP) and lower pressure (LP) rotors at high speed, the thermal behaviours are more prominent. The friction heat generation and convergence will make the temperature rise, seriously, the scuffing [2] and biting may occur if at a very high temperature. Hence, the inter-shaft bearings' thermal behaviours affected by dynamic properties of systems urgently need further investigations.

The thermal behaviours of rolling bearings have been studied by many researchers in the past decades. In 1945, an empirical formula about the friction heat generations of rolling bearings was pioneered by Palmgren [3] through a large number of experiments. Burton et al. [4] built a theoretical model for thermal failure in the case of dry or lightly-lubricated angular contact ball bearings to study the steady-state thermal behaviour rather than the transient behaviour. Sud et al. [5] studied the thermal behaviour of the angular contact ball bearings and thrust ball bearings under the preload experimentally. Harris [6] applied the basic laws of heat conduction and heat convection to the rolling bearing by lumped parameter method and predicted the steady-state temperatures of the rolling bearing main components, such as the inner ring, outer ring and rollers. Winer et al. [7] developed an analytical model of a tapered roller bearing and housing system, and calculated typical thermal resistances among the rotor parts. DeMul et al. [8, 9] presented a five-degree-of-freedom (5DOF) bearing model to analyze the load–deflection relationship in a matrix method. Based on which, Jorgensen and Shin [10] considered the thermal expansion to predict spindle/bearing performance at high speed and found the steady-state temperature distribution from a quasi-three-dimensional heat transfer model. Stein and Tu [11] utilized Palmgren's empirical formula to estimate the friction torque and carried out a comprehensive thermal analysis of the angular contact ball bearing. Kim and Lee [12] investigated the thermal and dynamic behaviours of a rotor-bearing system considering tolerance, cooling conditions and thermal deformation. Sun et al. [13] offered an approach, named as modal truncation augmentation method, to simulate the blade loss considering the thermal expansion, to achieve this, they built the heat transfer network and listed the thermal resistances. Jiang and Mao [14] set up an experiment rig to comparative study a high-speed hybrid ceramic and steel ball bearings with oil-air lubrication. Ma et al. [15] established a mathematical model to accurately calculate the FHGs of spherical roller bearings based on the local analysis approach. Takabi and Khonsari [16] proposed a complex heat transfer network of the bearing assembly to study the unsteady-state temperature of a deep-groove ball bearing in an oil-bath lubrication system, and verified the validity through experimental tests. Ai et al. [17] established the thermal network model for the double-row tapered roller bearing according to the generalized Ohm's law, and developed a static model to obtain force distribution and motion parameters of the roller bearing. Than and Huang [18] combined the static model with the finite element method as a unified method to predict nonlinear thermal behaviours of high-speed spindle bearings, and found that the temperature field of the spindle-bearing system was in good agreement with the experiment. Gao et al. [19] established a kinematic-Hertzian-thermo-hydro-dynamic (KH-THD) model to study the mechanism of the skid, over-skidding and negative-skidding phenomena, and found that there is a great temperature gradient inside the bearing. In all of the above works, they all focused on the supporting bearings rather than the inter-shaft bearings. It is essential to do some investigations on thermal behaviours of inter-shaft bearings because of their unique application.

Many researchers have studied the dynamics of a dual-rotor system with the inter-shaft bearing by far. Hibner [20] predicted the vibratory response of a two-shaft aircraft engine, with the aid of a unique transfer-matrix method, he illustrated the basic concepts of multi-shaft critical speeds and nonlinear viscous-damped response. Gupta et al. [21] built a dual-rotor test rig to investigate the dynamic properties of the dual-rotor system by simulating the two spool aircraft engine dynamically. A 2DOF simple but realistic model of the non-symmetric co-axial co-rotating or counter-rotating rotors was presented by Ferraris et al.

[22] to study the critical speeds and the dynamic responses caused by the unbalance through hand calculations. Guskov et al. [23] studied the unbalanced responses of a dual-rotor system, which is consisted of one LP shaft, one HP shaft and an inter-shaft bearing between them. In the research of Sun et al. [24], the MHB-AFT (Multi-Harmonic Balance combined with the Alternating Frequency/Time domain) method is applied to compute the steady-state dynamic response of an 8DOF dual-rotor system caused by the rub-impact, but the inter-shaft bearing is simplified into a linear spring. Based on which, Gao et al. [25] considered the inter-shaft bearing's nonlinear factors, such as the Hertzian contact and the clearance, and proposed a force model considering the local defect on outer and inner rings to investigate the dynamic behaviours of the simple 8DOF system. Unfortunately, in the above literature about the dual-rotor system, most of the inter-shaft bearings are simplified linearly, or even without considering the thermal effect of bearings.

This paper aims to investigate the effect of the dynamics of the dual-rotor system on the temperature of the inter-shaft bearing. Instead of the static load commonly used in previous literature, the dynamic load is employed to establish the unsteady-state heat balance equations of the inter-shaft bearing. Moreover, the dynamic load is able to mirror the dynamic properties of the system. Thus, the dynamics of the system is coupled with the heat transfer of the bearing. Furthermore, the viscosity-temperature relationship of the lubricant is considered in this model. Results show that the bearing's temperatures form two "temperature peak" in the "resonance zone" of the system, which indicates the dynamic properties of the system make an important impact on the bearing's temperatures.

2 Unsteady-state heat transfer model under the dynamic load

2.1 Dynamic load of the inter-shaft bearing

The structural diagram of a simple dual-rotor and an inter-shaft bearing system is shown in Fig. 1 [24, 25]. The LP and HP rotors are coupled by a radial cylindrical roller bearing, whose outer and inner rings whirl with HP and LP rotors. Where ω_1 is the LP rotor's rotation speed while ω_2 is the HP rotor's rotation speed. The rotation speed ratio $\lambda = \frac{\omega_2}{\omega_1}$ is constant during operation, where $\lambda > 1$ for co-rotating while $\lambda < -1$ for counter-rotating. Assume that the LP and HP rotors rotate at constant rotation speeds and the rotation speed ratio is constant, the DOFs of the rotational angles of LP and HP rotors around the z-axis can be ignored. Therefore, the simple dual-rotor system has 8DOFs, which are the vertical and horizontal displacements of LP and HP rotors x_1, y_1, x_2, y_2, and the rotational angles of LP and HP rotors around the vertical and horizontal axes θ_x, θ_y, φ_x, φ_y.

The structural diagram of a simple dual-rotor and an inter-shaft bearing system is shown in Fig. 1. The second kind of Lagrange's equation is applied to establish the dynamic equations of the system. Both LP and HP rotors are assumed as rigid rotors, the energies of the system [24–26] are:

The kinetic energy of the system is

$$\begin{aligned} T = &\frac{1}{2}m_1\left(\dot{x}_1^2 + \dot{y}_1^2\right) + \frac{1}{2}J_{d_1}\left(\dot{\theta}_x^2 + \dot{\theta}_y^2\right) \\ &+ \frac{1}{2}J_{p_1}\left(\omega_1^2 - 2\omega_1\theta_x\dot{\theta}_y\right) + \frac{1}{2}m_2\left(\dot{x}_2^2 + \dot{y}_2^2\right) \\ &+ \frac{1}{2}J_{d_2}\left(\dot{\varphi}_x^2 + \dot{\varphi}_y^2\right) + \frac{1}{2}J_{p_2}\left(\omega_2^2 - 2\omega_2\varphi_x\dot{\varphi}_y\right), \end{aligned} \tag{1a}$$

where m_1, m_2 are the mass of the LP and HP rotor; J_{p1}, J_{p2} are the polar moment of inertia of the LP and HP rotor; J_{d1}, J_{d2} are diameter moment of inertia of the LP and HP rotor.

The potential energy of the dual-rotor system is

$$\begin{aligned} V = &\frac{1}{2}k_1\left[\left(x_1 - \theta_y l_1\right)^2 + \left(y_1 + \theta_x l_1\right)^2\right] \\ &+ \frac{1}{2}k_2\left[\left(x_1 + \theta_y l_2\right)^2 + \left(y_1 - \theta_x l_2\right)^2\right] \\ &+ \frac{1}{2}k_3\left[\left(x_2 - \varphi_y l_3\right)^2 + \left(y_2 - \varphi_x l_3\right)^2\right] + m_1 g x_1 \\ &+ m_2 g x_2, \end{aligned} \tag{1b}$$

where k_{i} (i = 1, 2, 3) are stiffness of linear supports.

The dissipation energy of the dual-rotor system is

$$\begin{aligned} D = &\frac{1}{2}c_1\left[\left(\dot{x}_1 - \dot{\theta}_y l_1\right)^2 + \left(\dot{y}_1 + \dot{\theta}_x l_1\right)^2\right] \\ &+ \frac{1}{2}c_2\left[\left(\dot{x}_1 + \dot{\theta}_y l_2\right)^2 + \left(\dot{y}_1 - \dot{\theta}_x l_2\right)^2\right] \\ &+ \frac{1}{2}c_3\left[\left(\dot{x}_2 - \dot{\varphi}_y l_3\right)^2 + \left(\dot{y}_2 + \dot{\varphi}_x l_3\right)^2\right], \end{aligned} \tag{1c}$$

where c_{i} (i = 1, 2, 3) are damping of linear supports.

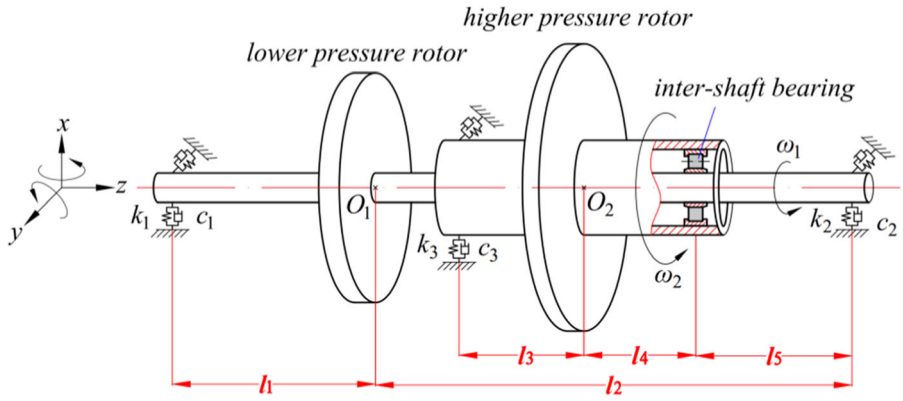

Fig. 1 Structural diagram of a simple dual-rotor and an inter-shaft bearing system

The virtual work of the dual-rotor system is

$$\begin{aligned}\delta W = {} & m_1\omega_1^2 e_1\cos(\omega_1 t)\delta x_1 + m_1\omega_1^2 e_1\sin(\omega_1 t)\delta y_1 \\ & + m_2\omega_2^2 e_2\cos(\omega_2 t)\delta x_2 + m_2\omega_2^2 e_2\sin(\omega_2 t)\delta y_2 \\ & - F_x\{\delta x_1 + \delta\theta_y(l_2 - l_5) - (\delta x_2 + \delta\varphi_y l_4)\} \\ & - F_y\{\delta y_1 - \delta\theta_x(l_2 - l_5) - (\delta y_2 - \delta\varphi_x l_4)\},\end{aligned} \tag{1d}$$

where e_1, e_2 are unbalances of the LP rotor and the HP rotor; δx_1, δy_1, δx_2, δy_2, $\delta\theta_x$, $\delta\theta_y$, $\delta\varphi_x$, $\delta\varphi_y$ are virtual displacements; F_x, F_y are the forces of the inter-shaft bearing along the vertical direction and horizontal direction.

Substitute Eqs. (1a–d) into the second kind Lagrange's equation, the dynamic equations of the dual-rotor system are obtained as:

$$\begin{aligned}& m_1\ddot{x}_1 + c_1\left(\dot{x}_1 - \dot{\theta}_y l_1\right) + c_2\left(\dot{x}_1 + \dot{\theta}_y l_2\right) \\ & + k_1\left(x_1 - \theta_y l_1\right) + k_2\left(x_1 + \theta_y l_2\right) \\ & = m_1\omega_1^2 e_1\cos(\omega_1 t) - F_x - m_1 g,\end{aligned} \tag{2a}$$

$$\begin{aligned}& m_1\ddot{y}_1 + c_1\left(\dot{y}_1 + \dot{\theta}_x l_1\right) + c_2\left(\dot{y}_1 - \dot{\theta}_x l_2\right) \\ & + k_1(y_1 + \theta_x l_1) + k_2(y_1 - \theta_x l_2) \\ & = m_1\omega_1^2 e_1\sin(\omega_1 t) - F_y,\end{aligned} \tag{2b}$$

$$\begin{aligned}& J_{d_1}\ddot{\theta}_x + \omega_1 J_{p_1}\dot{\theta}_y + c_1 l_1\left(\dot{y}_1 + \dot{\theta}_x l_1\right) - c_2 l_2\left(\dot{y}_1 - \dot{\theta}_x l_2\right) \\ & + k_1 l_1(y_1 + \theta_x l_1) - k_2 l_2(y_1 - \theta_x l_2) \\ & = F_y(l_2 - l_5),\end{aligned} \tag{2c}$$

$$\begin{aligned}& J_{d_1}\ddot{\theta}_y - \omega_1 J_{p_1}\dot{\theta}_x - c_1 l_1\left(\dot{x}_1 - \dot{\theta}_y l_1\right) + c_2 l_2\left(\dot{x}_1 + \dot{\theta}_y l_2\right) \\ & - k_1 l_1\left(x_1 - \theta_y l_1\right) + k_2 l_2\left(x_1 + \theta_y l_2\right) \\ & = -F_x(l_2 - l_5),\end{aligned} \tag{2d}$$

$$\begin{aligned}& m_2\ddot{x}_2 + c_3\left(\dot{x}_2 - \dot{\varphi}_y l_3\right) + k_3\left(x_2 - \varphi_y l_3\right) \\ & = m_2\omega_2^2 e_2\cos(\omega_2 t) + F_x - m_2 g,\end{aligned} \tag{2e}$$

$$\begin{aligned}& m_2\ddot{y}_2 + c_3(\dot{y}_2 + \dot{\varphi}_x l_3) + k_3(y_2 + \varphi_x l_3) \\ & = m_2\omega_2^2 e_2\sin(\omega_2 t) + F_y,\end{aligned} \tag{2f}$$

$$\begin{aligned}& J_{d_2}\ddot{\varphi}_x + \omega_2 J_{p_2}\dot{\varphi}_y + c_3 l_3(\dot{y}_2 + \dot{\varphi}_x l_3) + k_3 l_3(y_2 + \varphi_x l_3) \\ & = -F_y l_4,\end{aligned} \tag{2g}$$

$$\begin{aligned}& J_{d_2}\ddot{\varphi}_y - \omega_2 J_{p_2}\dot{\varphi}_x - c_3 l_3\left(\dot{x}_2 - \dot{\varphi}_y l_3\right) - k_3 l_3\left(x_2 - \varphi_y l_3\right) \\ & = F_x l_4,\end{aligned} \tag{2h}$$

Equations (2a–h) in the matrix form is

$$M\ddot{X} + C\dot{X} + KX = F, \tag{3}$$

where the variable vector $\boldsymbol{X} = [x_1 \quad y_1 \quad \theta_x \quad \theta_y x_2 y_2 \varphi_x \varphi_y]^{\mathrm{T}}$; M, C, K, are the mass matrix, the damping matrix, the stiffness matrix; P is the external force vector.

The inter-shaft bearing is the nonlinear factors of the dynamic equations, such as the fractional exponential of Hertzian contact and the clearance. Figure 2 displays the inter-shaft bearing's kinetic diagram.

The angular position of the kth roller at any time t is expressed as

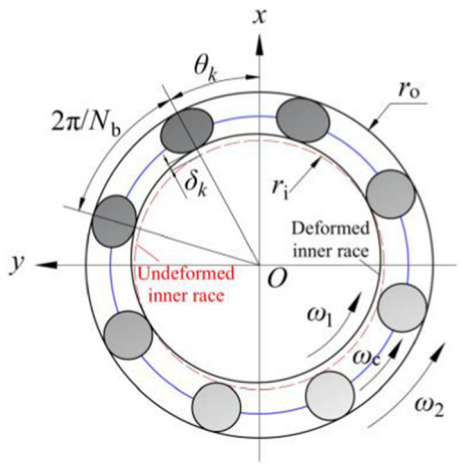

Fig. 2 The inter-shaft bearing's kinetic diagram

$$\theta_k = \frac{2\pi}{N_b}(k-1) + \omega_c t \quad (k = 1, 2, \cdots, N_b), \tag{4}$$

where $\omega_c = \frac{\omega_1 r_i + \omega_2 r_o}{r_i + r_o}$ represents the cage's rotation speed, where r_i, r_o represents the radiuses of the inner ring and the outer ring.

The relative deformation between kth roller and rings is

$$\begin{aligned}\delta_k &= (x_i - x_o)\cos\theta_k + (y_i - y_o)\sin\theta_k \\ &\quad - \delta_0 \ (k = 1, 2, \cdots, N_b), \\ &= \left\{\left[x_1 + \theta_y(l_2 - l_5)\right] - \left(x_2 + \varphi_y l_4\right)\right\}\cos\theta_k \\ &\quad + \left\{\left[y_1 - \theta_x(l_2 - l_5)\right] - \left(y_2 - \varphi_x l_4\right)\right\}\sin\theta_k - \delta_0,\end{aligned} \tag{5}$$

where $2\delta_0$ is the radial clearance of the bearing; x_i, y_i, x_o, y_o are vertical displacement and horizontal displacement of the inner and outer rings.

The forces of the inter-shaft bearing [26] are

$$\begin{bmatrix} F_x \\ F_y \end{bmatrix} = K_b \sum_{k=1}^{N_b} \delta_k^{10/9} H(\delta_k) \begin{bmatrix} \cos\theta_k \\ \sin\theta_k \end{bmatrix}, \tag{6}$$

where $H(\cdot) = \begin{cases} 1 & (\cdot > 0) \\ 0 & (\cdot \le 0) \end{cases}$ denotes the step function, K_b represents the stiffness and N_b represents the roller number of bearing.

The RMS, namely, root mean square [27, 28], is applied to compute the dynamic load of the bearing. The RMS can reflect the energy of the dynamic load, thus, RMS is more proper to compute the dynamic load than the P-P (peak-peak) value. The dynamic load can be expressed as

$$\begin{aligned} F_b &= \sqrt{\frac{\int_0^T \left(\left(F_x(t) - \overline{F}_x\right)^2 + \left(F_y(t) - \overline{F}_y\right)^2\right) dt}{T}} \\ &= \sqrt{\frac{\sum_{i=1}^{N} \left(\left(F_x(i) - \overline{F}_x\right)^2 + \left(F_y(i) - \overline{F}_y\right)^2\right)}{N}}, \end{aligned} \tag{7}$$

where T denotes the period of forces; N denotes the discretization points number; $\overline{F}_x$, $\overline{F}_y$ are the averages of forces.

This research takes the NU1020 bearing for example to investigate the thermal behaviours of the inter-shaft bearing, and Table 1 lists the parameters of the NU1020 bearing.

The dynamic parameters of the system are displayed below:

$m_1 = 97.37\,\text{kg}$, $J_{p1} = 3.6907\,\text{kg}\cdot m^2$, $J_{d1} = 1.8454\,\text{kg}\cdot m^2$, $m_2 = 108.30\,\text{kg}$, $J_{p2} = 4.0119\,\text{kg}\cdot\text{m}^2$, $J_{d2} = 2.0060\,\text{kg}\cdot\text{m}^2$, $k_1 = k_2 = k_3 = 6\times 10^7\,\text{N/m}$, $c_1 = c_2 = c_3 = 655\,\text{N}\cdot/m$, $l_1 = 0.9188\,\text{m}$, $l_2 = 1.1122\,\text{m}$, $l_3 = 0.5120\,\text{m}$, $l_4 = 0.6243\,\text{m}$, $l_5 = 0.0995\,\text{m}$, $\lambda = 1.2$, $e_1 = 3\,\mu m$, $e_2 = 2\,\mu m$.

Table 1 Parameters of the radial cylindrical roller bearing NU1020

Parameters	Values
Mass of rollers m_r	0.4748 kg
Mass of inner ring m_i	0.3912 kg
Mass of outer ring m_o	0.6250 kg
Nominal bore d	100 mm
Diameter of inner ring d_i	113 mm
Pitch diameter D_m	125 mm
Diameter of outer ring d_o	137 mm
Nominal outer diameter D	150 mm
Width B	24 mm
Roller diameter d_r	12 mm
Roller length a_r	14 mm
Roller number N_b	24
Radial clearance $2\delta_0$	10 μm
Stiffness K_b	10^8 N/m$^{10/9}$

Table 2 The experimental data of the kinematic viscosity at different temperatures [18]

Temperature T_L (°C)	30	40	50	60	70	80
Kinematic viscosity v (mm^2/s)	15	10	7.8	5.9	5	4

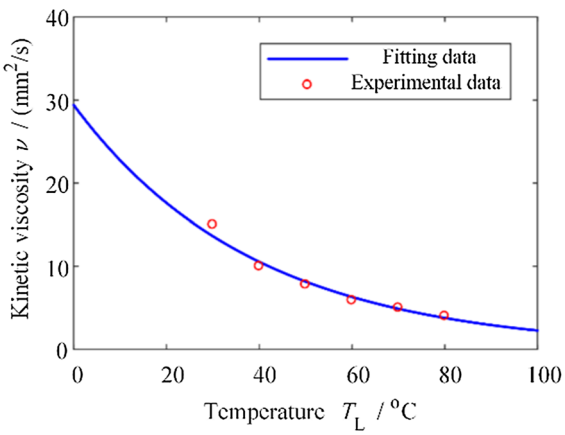

Fig. 3 The viscosity-temperature relationship of the lubricant

2.2 2.2 FHG under the dynamic load.

An empirical formula, presented by Palmgren [3], is utilized to compute the inter-shaft bearing's friction torques. The total friction torque M_t (N•mm) is consisted of two portions, one is the friction torque due to load M_b and the other is the friction torque due to viscosity M_v, as

$$M_t = M_b + M_v, \tag{8a}$$

Comparing with the static load [18] commonly used in previous literature, the dynamic load F_b is able to mirror the dynamic properties of the system, which enables the dynamic load more proper to depict the inter-shaft bearing's practical load especially in the "resonance zone" of the system. Therefore, the dynamic load is applied to compute the friction torque due to load as

$$M_b = f_b F_b D_m, \tag{8b}$$

where f_b is a factor depended on bearing type and load, $f_b = 0.0002 \sim 0.0004$ for the radial cylindrical roller bearings with cages [6]; D_m is the pitch diameter.

The friction torque due to viscosity is

$$M_v = \begin{cases} 10^{-7} f_v (v \cdot \Delta n)^{2/3} D_m^3 & v \cdot \Delta n \geq 2000 \\ 160 \times 10^{-7} f_v D_m^3 & v \cdot \Delta n < 2000 \end{cases}, \tag{8c}$$

where f_v is a factor depended on bearing type and lubrication method, for radial cylindrical roller bearings with cages, $f_v = 0.6 \sim 1$ for grease, $f_v = 1.5 \sim 2.8$ for oil mist, and $f_v = 2.2 \sim 4$ for oil bath [6]; v is the kinematic viscosity of the lubricant (mm^2/s), which is a function of the temperature; $\Delta n = \frac{60}{2\pi}|\omega_2 - \omega_1| = \frac{60}{2\pi}|\lambda - 1|\omega_1$ is the difference of rotation speeds (r/min), which is much more complex than the single rotor system.

The total FHG (W) under the dynamic load is

$$Q_t = Q_b + Q_v, \tag{9a}$$

the load FHG under the dynamic load is

$$Q_b = 10^{-3}|\omega_2 - \omega_1| M_b = 10^{-3}|\lambda - 1|\omega_1 M_b, \tag{9b}$$

the viscosity FHG is

$$Q_v = 10^{-3}|\omega_2 - \omega_1| M_v = 10^{-3}|\lambda - 1|\omega_1 M_v, \tag{9c}$$

The viscosity of the lubricant is regarded as a function of temperature because the temperature makes an important impact on the viscosity. The viscosity-temperature relationship of the lubricant should be considered for the viscosity FHG. The experimental data of the kinematic viscosity at different temperatures [18] are shown in Table 2.

The Reynolds' model of viscosity-temperature relationship [29] is

$$v = v_0 e^{-\gamma(T - T_0)}, \tag{10}$$

where γ is the viscosity-temperature coefficient, $\gamma = 0.018 \sim 0.036\,^{\circ}\mathrm{C}^{-1}$ for mineral oil; T_0, ν_0 are the initial temperature and the initial kinematic viscosity.

The Reynolds' model is applied to fit the experimental data [18] in Table 2, the fitting curve is shown in Fig. 3. The viscosity-temperature coefficient is $\gamma = 0.0256\,^{\circ}\mathrm{C}^{-1}$, which indicates the Reynolds' model is appropriate for the viscosity-temperature relationship of the lubricant. Moreover, the kinematic viscosity decreases greatly as the temperature rises, which further confirms the importance of the viscosity-temperature relationship.

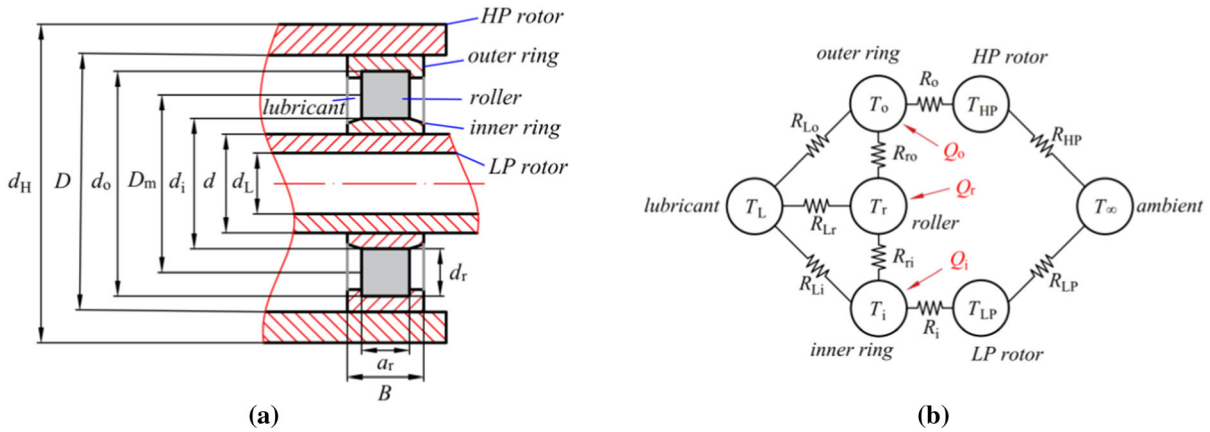

Fig. 4 Inter-shaft bearing's structure size and heat transfer network. **a** Structure size. **b** Heat transfer network

2.3 Unsteady-state heat transfer model under the dynamic load

The material of bearings is bearing steel GCr15, thus, Biot numbers of the outer ring, the inner ring and cylindrical rollers, are small enough ($Bi<0.1$). The lumped parameter method, i.e. lumped heat capacity method [30], can be used for the heat transfer modelling for the bearing. The structure size and the heat transfer network of the inter-shaft bearing are shown in Fig. 4, where d_L, d, d_i, D_m, d_o, D, d_H are the diameters; B, d_r, a_r are the width, the diameter of the roller, the length of the roller; T_r, T_i, T_o, T_{LP}, T_{HP}, T_L, T_∞ are the temperatures; R_{ri}, R_{ro}, R_i, R_o are the heat conduction thermal resistances; R_{Lr}, R_{Li}, R_{Lo}, R_{LP}, R_{HP} are the heat convection thermal resistances.

Assume that the temperature of the lubricant is $T_L=\frac{T_r+T_i+T_o}{3}$ [11], and an average partition coefficient [11] is applied as follows:

$$Q_t = Q_r + Q_i + Q_o, \tag{11a}$$

$$Q_r = 0.5\,Q_t, \tag{11b}$$

$$Q_i = 0.25\,Q_t, \tag{11c}$$

$$Q_o = 0.25\,Q_t, \tag{11d}$$

where Q_r is the FHG distributed to rollers, Q_i is the FHG distributed to the inner ring and Q_o is the FHG distributed to the outer ring.

According to the generalized Ohm's law [17], the unsteady-state heat balance equations are derived as

$$\frac{T_i-T_r}{R_{ri}}+\frac{T_o-T_r}{R_{ro}}+\frac{T_L-T_r}{R_{Lr}}+Q_r=m_r c_{steel}\frac{\partial T_r}{\partial t}, \tag{12a}$$

$$\frac{T_r-T_i}{R_{ri}}+\frac{T_{LP}-T_i}{R_i}+\frac{T_L-T_i}{R_{Li}}+Q_i=m_i c_{steel}\frac{\partial T_i}{\partial t}, \tag{12b}$$

$$\frac{T_r-T_o}{R_{ro}}+\frac{T_{HP}-T_o}{R_o}+\frac{T_L-T_o}{R_{Lo}}+Q_o=m_o c_{steel}\frac{\partial T_o}{\partial t}, \tag{12c}$$

$$\frac{T_i-T_{LP}}{R_i}+\frac{T_\infty-T_{LP}}{R_{LP}}=m_{LP} c_{steel}\frac{\partial T_{LP}}{\partial t}, \tag{12d}$$

$$\frac{T_o-T_{HP}}{R_o}+\frac{T_\infty-T_{HP}}{R_{HP}}=m_{HP} c_{steel}\frac{\partial T_{HP}}{\partial t}, \tag{12e}$$

where t is time; c_{steel} is the specific heat capacity of steel; m_r, m_i, m_o are the mass of rollers, the inner ring, the outer ring; $m_{LP}=\frac{\pi}{4}\rho_{steel}\left(d^2-d_L^2\right)B$ is the mass of the part of LP rotor contact the inner ring, where ρ_{steel} is the density of the steel; $m_{HP}=\frac{\pi}{4}\rho_{steel}\left(d_H^2-D^2\right)B$ is the mass of the part of HP rotor contact the outer ring; the thermal resistance between the inner ring and the LP rotor $R_i=\frac{\ln(d_i/d_L)}{2\pi k_{steel}B}$, the thermal resistance between the outer ring and the HP rotor $R_o=\frac{\ln(d_H/d_o)}{2\pi k_{steel}B}$; the thermal resistance between rollers and the inner ring $R_{ri}=\frac{R_{ri}^{one}}{n_b}$, the thermal resistance between rollers and the outer ring $R_{ro}=\frac{R_{ro}^{one}}{n_b}$, herein n_b is the average pressed roller number [31], $R^{one}=\frac{1.13}{k_{steel}\sqrt{A_r\cdot Pe^*}}$ is the

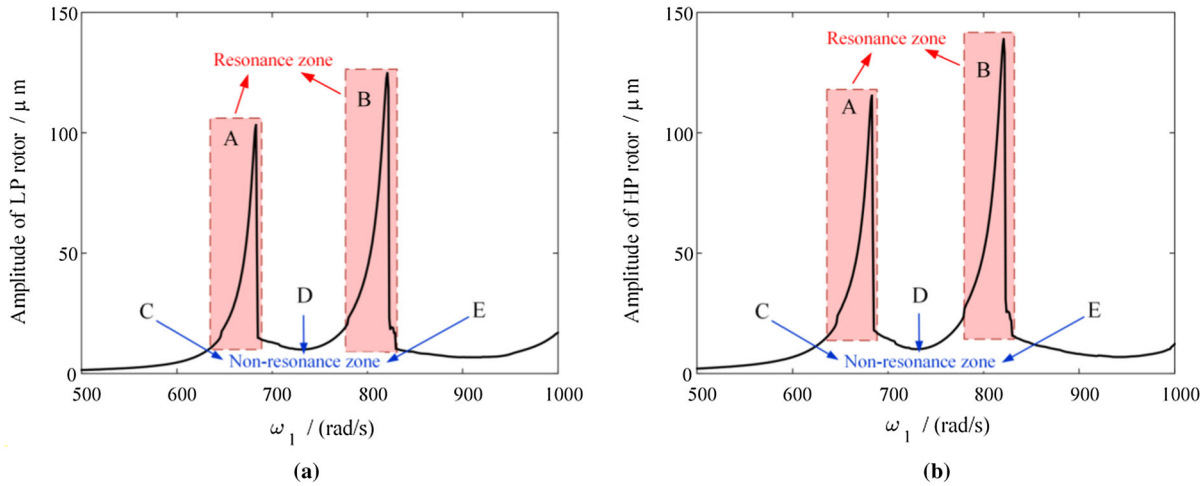

Fig. 5 Amplitude frequency curve of the dual-rotor system. **a** The LP rotor. **b** The HP rotor

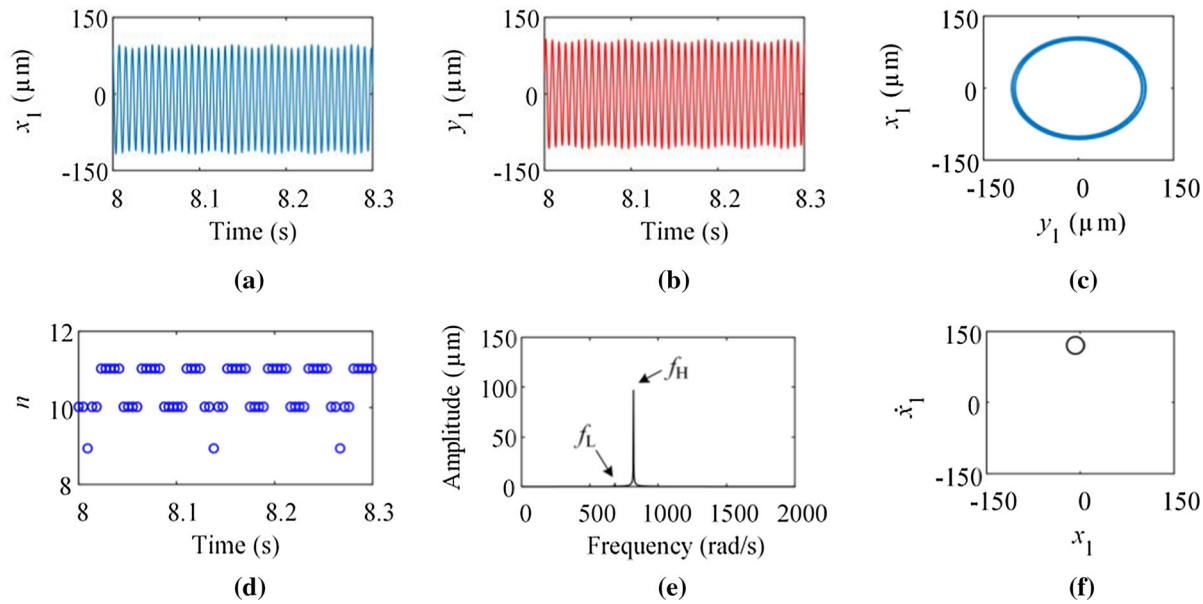

Fig. 6 Dynamic responses analysis for ω_1 = 683 rad/s in A. **a** The vertical displacement history. **b** The horizontal displacement history. **c** The orbit of LP rotor. **d** The number of pressed rollers. **e** Spectrum diagram. **f** Poincaré diagram

thermal resistance between one roller and the corresponding ring, A_r is the area of the interface between corresponding ring and roller, Pe^* is the modified Peclet number [32].

The thermal resistance of heat convection can be derived by the Nusselt number Nu because of

$$R_v = \frac{1}{A_v h} = \frac{1}{A_v} \cdot \frac{L}{k \cdot Nu}, \tag{13}$$

where A_v is the area of heat convection; h is the convective heat transfer coefficient; k is the thermal conductivity of the fluid; L is the characteristic length. The heat convection thermal resistances R_{Lr}, R_{Li}, R_{Lo}, R_{LP}, R_{HP} can be calculated according to Eq. (13).

(1) The thermal resistance between the lubricant and the rollers R_{Lr}.F and [33] offered a better correlation, instead of the McAdams correlation, to

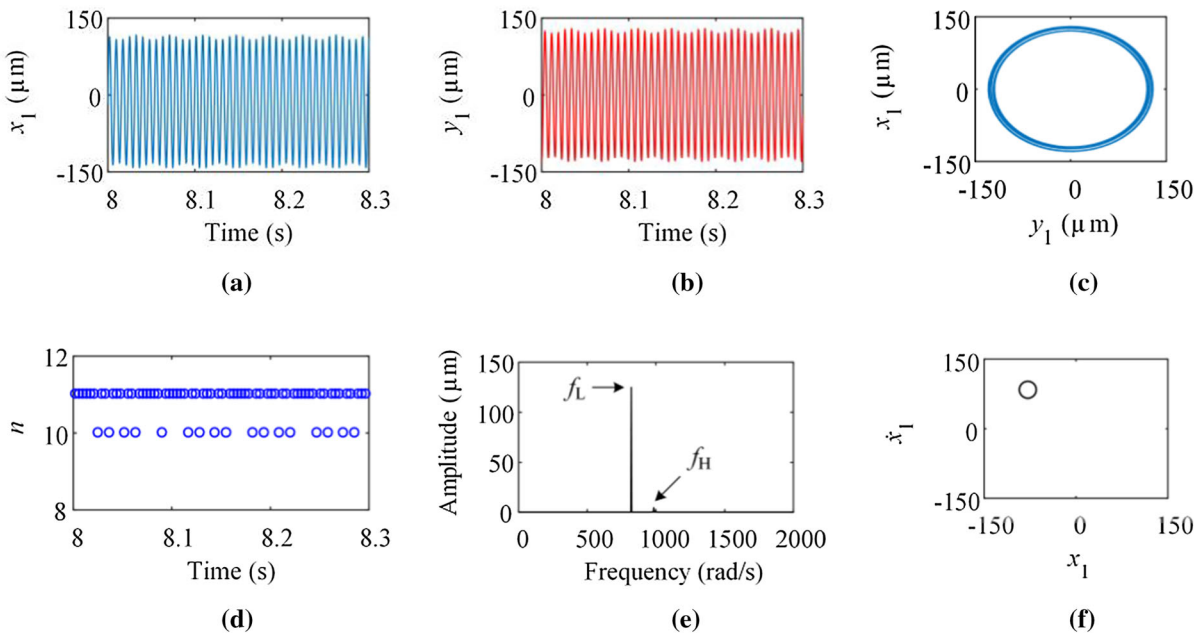

Fig. 7 Dynamic responses analysis for ω_1 = 821 rad/s in B. **a** The vertical displacement history. **b** The horizontal displacement history. **c** The orbit of LP rotor. **d** The number of pressed rollers. **e** Spectrum diagram. **f** Poincaré diagram

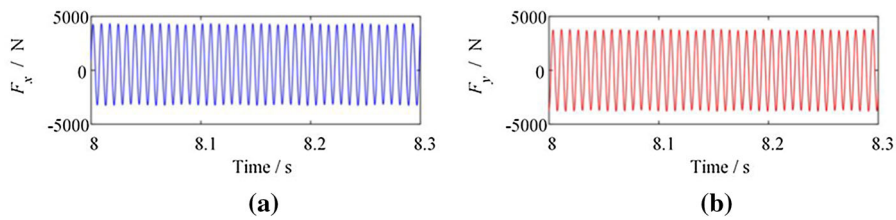

Fig. 8 Inter-shaft bearing's forces for ω_1 = 683 rad/s in A. **a** Vertical direction. **b** Horizontal direction

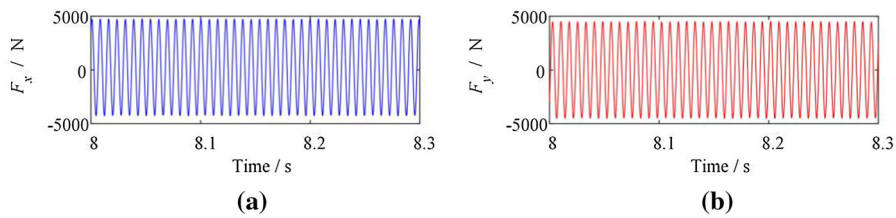

Fig. 9 Inter-shaft bearing's forces for ω_1 = 821 rad/s in B. **a** Vertical direction. **b** Horizontal direction

represent the experimental data for the forced convection from a cylinder to the liquid in cross-flow, as

$$Nu = \left(0.35 + 0.34\,\mathrm{Re}^{0.5} + 0.15\,\mathrm{Re}^{0.58}\right)\mathrm{Pr}^{0.3}, \quad (14)$$

where $Re = \frac{VL}{\nu}$ is the Reynolds number of the liquid; $Pr = \frac{\nu}{\alpha}$ is the Prandtl number, herein α is the thermal diffusivity. The correlation is valid for $10^{-1} < Re < 10^5$.

(2) The thermal resistance between the lubricant and the inner ring (the outer ring) R_{Li} (R_{Lo}) Gazley [34]

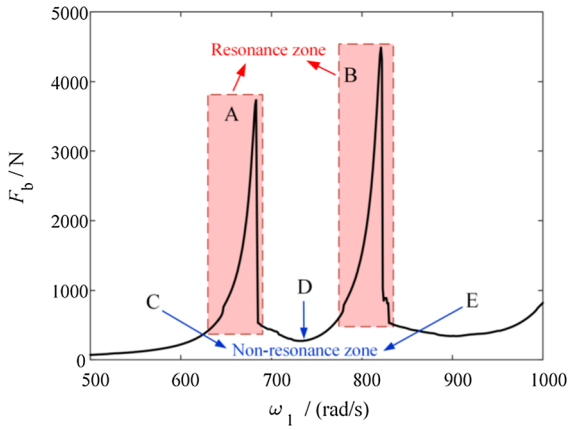

Fig. 10 The dynamic load of the inter-shaft bearing against the rotation speed

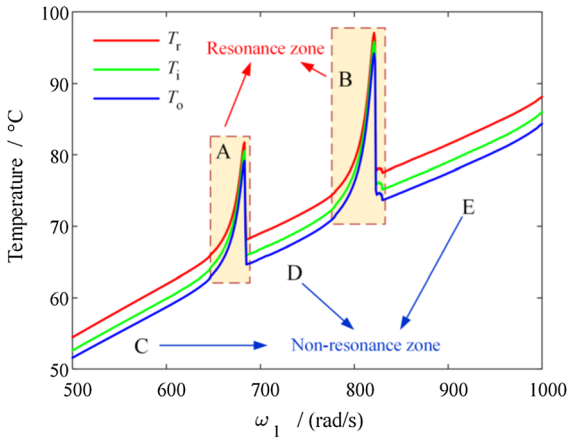

Fig. 11 Steady-state temperature of the rollers, the inner ring and the outer ring against the LP rotor's rotation speed

and Bjorklund [35] studied the heat convection of two rotating concentric cylinders, which were separated by the mixture of grease-air. The inner race and the outer race can be seen as two rotating concentric cylinders separated by the lubricant, the correlation is

$$Nu = \begin{cases} 2 & Ta < 41 \\ 0.167\, Ta^{0.69}\, \mathrm{Pr}^{0.4} & 41 \le Ta < 100 \\ 0.401\, Ta^{0.5}\, \mathrm{Pr}^{0.4} & 100 < Ta \end{cases}, \quad (15)$$

where $Ta = Re\sqrt{\frac{\delta_{io}}{r}}$ is the Taylor number, in which $\delta_{io} = \frac{d_o - d_i}{2}$ is the distance from the outer ring to the inner ring.

(3) The thermal resistance between the LP (HP) rotor and the ambient R_{LP} (R_{HP}) Yang [36] studied the heat convection between rotors and the ambient are forced convection due to the rotation of shafts, and offered the correlation as

$$Nu = \begin{cases} 0.00308\,\mathrm{Re} + 4.432 & \mathrm{Re} < 7300 \\ \mathrm{Re}^{0.37} & 7300 \le \mathrm{Re} < 9600 \\ 30.5\,\mathrm{Re}^{-0.0042} & 9600 < \mathrm{Re} \end{cases}, \quad (16)$$

3 Results and discussions

3.1 Dynamic load

Dynamic responses of Eqs. (2a–h) and Eq. (6) can be easily obtained by fourth order Runge–Kutta method. The initial state for $\omega_1 = 500$rad/s is $\begin{bmatrix} \boldsymbol{X} & \dot{\boldsymbol{X}} \end{bmatrix} = \begin{bmatrix} \boldsymbol{0} & \boldsymbol{0} \end{bmatrix}$, while for subsequent rotation speed, the initial state is the final state of the previous rotation speed. The calculation time is given as 10 s, which is long enough for the system to reach steady-state responses. The time step is given as 10^{-3} s, which is small enough to achieve accurate results. The errors are set as $< 10^{-6}$. The RMS of the horizontal and vertical displacements in a period is utilized to represent the vibration amplitude of the numerical results. The amplitude frequency curves of the LP rotor and the HP rotor are shown in Fig. 5.

Comparing Fig. 5a and Fig. 5b, it can be discovered that the two amplitude frequency curves are basically the same as each other, while the amplitude of the HP rotor is slightly greater than that of the LP rotor. Moreover, the amplitude increases so sharply in regions A and B that two peaks are formed here, while the amplitude is very small in other regions C, D and E. Thus, regions A and B are "resonance zone" and other regions C, D and E are "non-resonance zone".

In order to analyze the mechanism of "resonance zone" A and B in detail, Fig. 6 and Fig. 7 are dynamic responses analysis for ω_1 = 683 rad/s in A and ω_1 = 821 rad/s in B, including the vertical displacement history, the horizontal displacement history, the orbit diagram of the LP rotor, the pressed roller number, the spectrum diagram of the LP rotor's horizontal vibration signal and the Poincaré diagram. Herein, f_L, f_H are the unbalance frequencies of LP and HP rotors.

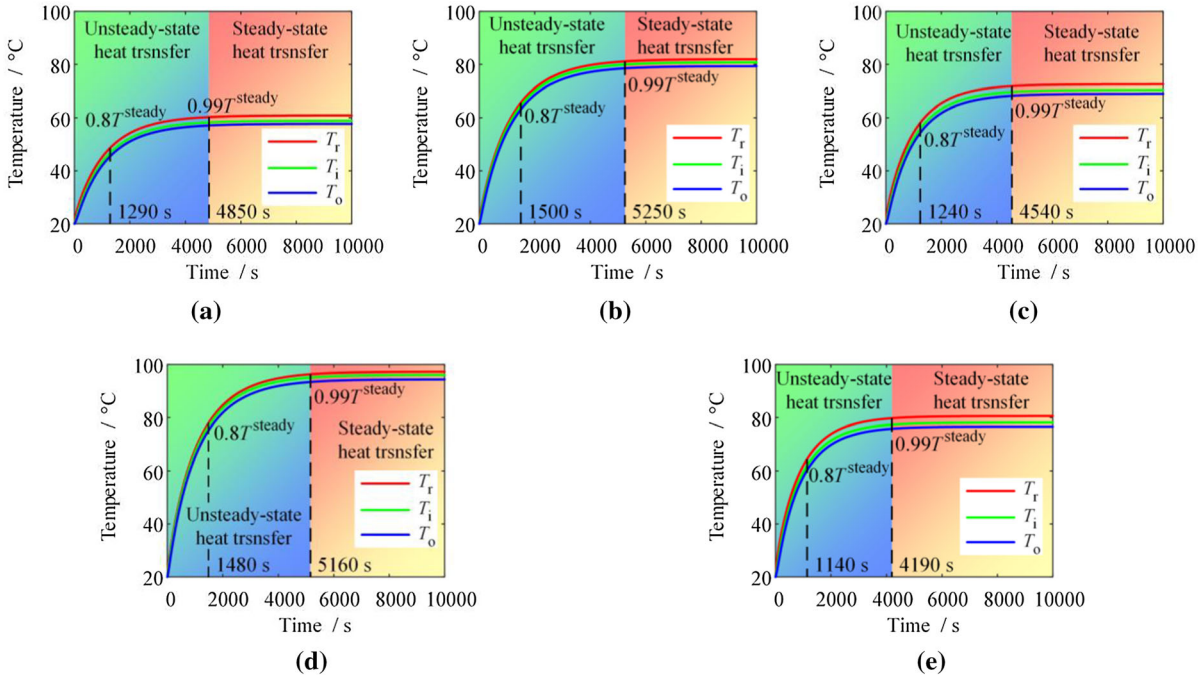

Fig. 12 Temperature evolutions of rollers, inner ring and outer ring. **a** For ω_1 = 600 rad/s in C. **b** For ω_1 = 683 rad/s in A. **c** For ω_1 = 750 rad/s in D. **d** For ω_1 = 821 rad/s in B. **e** For ω_1 = 900 rad/s in E

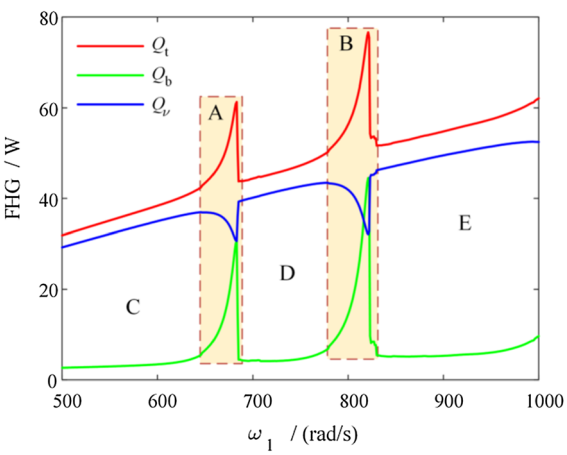

Fig. 13 FHGs against the LP rotor's rotation speed

For Fig. 6, the rotation speed ω_1 = 683 rad/s is located in the "resonance zone" A, f_H is the dominant frequency of the dynamic responses, f_L is very small. The vertical signal and the horizontal signal seem like beat vibration, the orbit of the LP rotor looks almost circular and there is only one point in the Poincaré diagram. The number of pressed rollers is time-varying from 9 to 11. Thus, the "resonance zone" A is induced by the HP rotor's unbalance.

For Fig. 7, the rotation speed ω_1 = 821 rad/s is located in the "resonance zone" B, f_L is the dominant frequency of the dynamic responses, f_H is very small. The vertical signal and the horizontal signal seem like beat vibration, the orbit of the LP rotor looks almost circular and there is only one point in the Poincaré diagram. The number of pressed rollers is time-varying between 10 and 11. Thus, the "resonance zone" B is induced by the LP rotor's unbalance.

Figures 8 and 9 are the inter-shaft bearing's forces of for ω_1 = 683 rad/s in A and for ω_1 = 821 rad/s in B. It can be seen that the vertical and horizontal forces are time-varying just like sine curves. Therefore, it is very difficult to substitute the forces into Eq. (8b) to compute M_b.

Once the dynamic equations Eqs. (2a–h) are solved, the inter-shaft bearing's forces along the vertical direction and horizontal direction are also attained at the same time. Based on Eq. (7), the dynamic load can be attained accordingly. Figure 10 displays the dynamic load varies with the LP rotor's rotation speed.

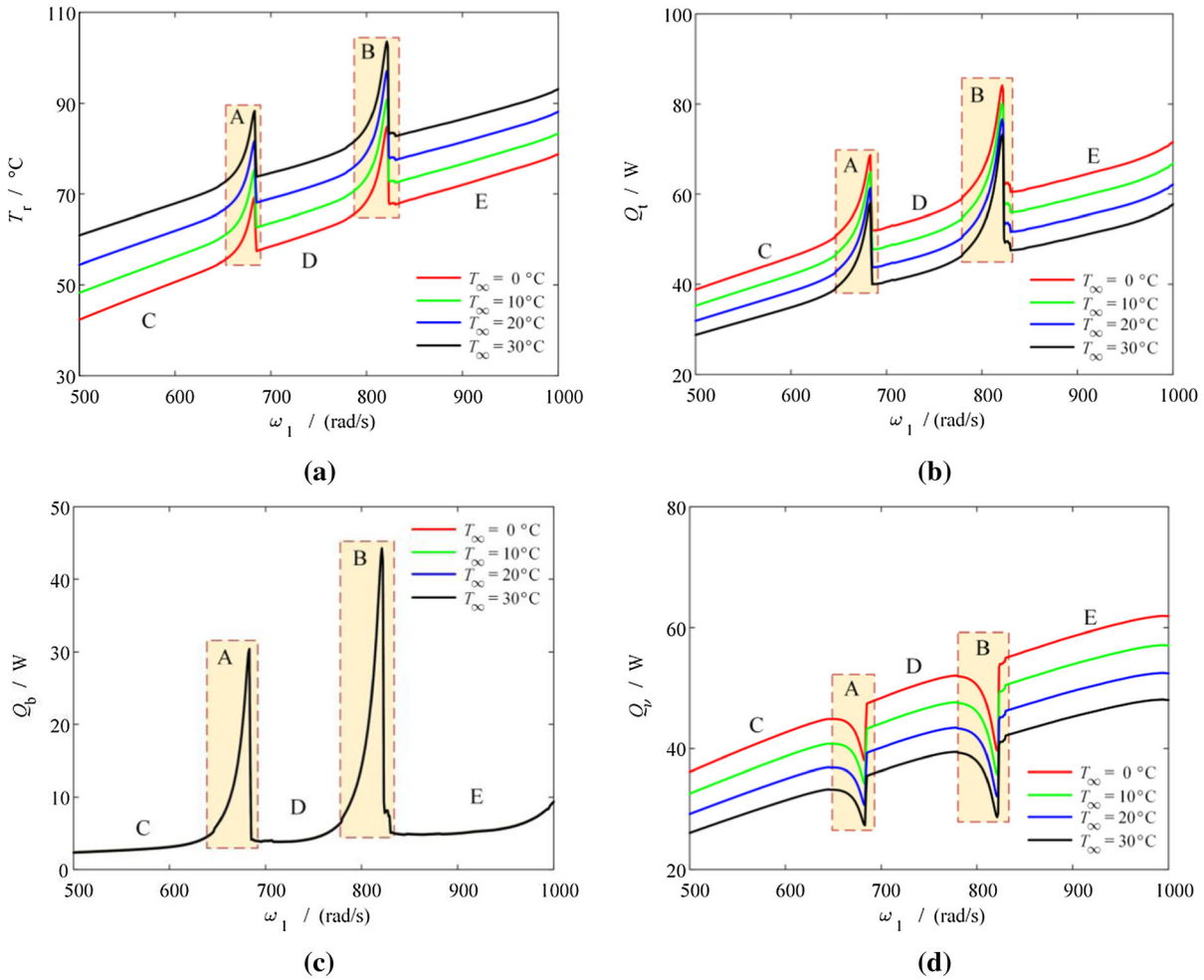

Fig. 14 Steady-state temperature and FHGs against the LP rotor's rotation speed at different ambient temperature. **a** Steady-state temperature of rollers. **b** Total FHG. **c** Load FHG. **d** Viscosity FHG

In Fig. 10, the dynamic load increases so sharply in the "resonance zone" A and B that two peaks are formed here, while the dynamic load is very small in the "non-resonance zone" C, D and E. Comparing Figs. 5 and 10, the dynamic load curve are basically the same with the amplitude frequency curves.

All in all, the dynamic load is able to mirror the dynamic properties of the dual-rotor system. Comparing with the static load commonly used in previous literature, the dynamic load is more proper to depict the practical load of the inter-shaft bearing especially in the "resonance zone" of the system because it contains the dynamic properties of the system. Comparing with the time-varying forces of the bearing, the dynamic load is not time-varying but constant for any rotation speed, which enables it easier to compute the load FHG.

3.2 Thermal analysis

The unsteady-state heat balance equations Eq. (12) also can be solved by the Runge–Kutta method. The initial temperature is equal to the ambient temperature $T_\infty = 20\,^{\circ}\mathrm{C}$; the calculation time is 10000 s, which is long enough for the inter-shaft bearing to reach steady-state temperatures; the time step is 10 s; the errors are $< 10^{-6}$. The kinematic viscosity of the lubricant is changing as Fig. 3 during the temperature evolution. Figure 11 displays the steady-state temperature of rollers, inner ring and outer ring vary with the LP rotor's rotation speed.

In Fig. 11, it can be discovered that the rollers' temperature T_r is highest and the outer ring's temperature T_o is lowest. T_o is lower than the inner ring's temperature T_i because the heat dissipation of the outer ring is stronger than that of the inner ring. Moreover, the variation for T_r, T_i and T_o with the rotation speed are the same with each other. In regions A and B, they all increase so sharply that two "temperature peak" are formed here. In regions C, D and E, they all increase gradually. Comparing Fig. 11 with Fig. 10, it can be discovered that A and B are exactly the "resonance zone" A and B of the dual-rotor system, while C, D and E are exactly the "non-resonance zone" C, D and E of the dual-rotor system.

In order to analyze the unsteady-state temperatures of rollers, the inner ring and outer ring in "resonance zone" and "non-resonance zone", Fig. 12 displays the temperature evolutions of the rollers, the inner ring and the outer ring for five different rotation speeds in "resonance zone" A, B and "non-resonance zone" C, D, E. Herein, T^{steady} represents the ideal steady-state temperature, 0.99 T^{steady} is taken as the boundary between the unsteady-state heat transfer and the steady-state heat transfer.

In Fig. 12, there is $T_r > T_i > T_o$ during the entire evolution. Initially, the rate of temperature rise is the highest, and it decreases over time. Finally, the rate of temperature rise decreases to zero, which means that the temperature reaches a steady-state temperature and no longer changes. The temperature rises quickly from the ambient temperature to 0.8 T^{steady}, but when the temperature further rises to 0.99 T^{steady}, the time consumed will increase sharply. Comparing the rotation speeds and the temperature in "resonance zone" A, B and "non-resonance zone" C, D, E, there is $\omega_C < \omega_A < \omega_D < \omega_B < \omega_E$ and $T_C < T_D < T_E < T_A < T_B$. As the rotation speed increases, the temperature does not simply increase monotonically. It indicates the dynamic properties of the dual-rotor system make an important impact on the temperature of the inter-shaft bearing.

In short, the dynamic behaviours of the dual-rotor system are coupled with the thermal behaviours of the inter-shaft bearing. In the "resonance zone" of the system, the temperature of bearing increases so sharply that two "temperature peak" are formed just like "resonance peak". In the "non-resonance zone" of the system, the temperature increases gradually.

3.3 FHG analysis

The effect of the rotation speed on the FHGs of the inter-shaft bearing is discussed in this section. The root cause of the temperature rise or fall is the accumulation or dispersion of heat. In order to find out the reason why the formation of temperature peaks in the "resonance zone" A and B, the FHG analysis is essential. Figure 13 displays the total FHG, the load FHG and the viscosity FHG vary with the LP rotor's rotation speed.

In Fig. 13, it can be discovered that the load FHG Q_b increases so sharply in "resonance zone" A and B that two peaks are formed here because the system resonates in A and B and the dynamic load is very large here; Q_b is very small in the "non-resonance zone" C, D and E. The load FHG is basically the same as the dynamic load. The viscosity FHG Q_v decreases so obviously in A and B that two valleys are formed here, because the temperature is higher and the lubricant viscosity is lower here; Q_v increases gradually in C, D and E. Therefore, the total FHG Q_t increases so sharply in "resonance zone" A and B that two peaks are formed here, while increases gradually in C, D and E.

It is worth noting that the total FHG shows the same behaviours with the inter-shaft bearing's temperatures. In the "resonance zone" A and B, the load FHG plays a leading role because the dynamic load increases rapidly here. In the "non-resonance zone" C, D and E, the viscosity FHG plays a leading role because the dynamic load is very small here. In the "resonance zone" A and B, the load FHG forms two peaks while the viscosity FHG forms two valleys.

3.4 Influence of the ambient temperature

This section discussed the temperature and the FHGs affected by the ambient temperature, which are $T_\infty = 0\,^{\circ}C$, $T_\infty = 10\,^{\circ}C$, $T_\infty = 20\,^{\circ}C$ and $T_\infty = 30\,^{\circ}C$, respectively. Figure 14 displays the comparison of the steady-state temperature of rollers, the total FHG, the load FHG and the viscosity FHG at different ambient temperature. In Fig. 14a, it can be seen that as T_∞ increases, T_r in both "resonance zone" and "non-resonance zone" increases gradually, it looks like the curve moves upward. In Fig. 14b, as T_∞ increases, Q_t in both "resonance zone" and "non-resonance zone" decreases gradually, it looks like the

curve moves downward. In Fig. 14c, it can be discovered that T_∞ does not affect the Q_b. In Fig. 14d, as T_∞ increases, Q decreases gradually, it looks like the curve moves downward.

In a word, the ambient temperature has an opposite effect on the temperature and the total FHG. As the ambient temperature increase, the temperature-rotation speed curve moves upward, while the total FHG-rotation speed curve moves downward. The ambient temperature has little effect on the load FHG but makes an important impact on the viscosity FHG because the viscosity-temperature relationship of the lubricant is considered.

4 Conclusion

In this research, FHGs under the inter-shaft bearing's dynamic load have been obtained by Palmgren's empirical formula, subsequently, the unsteady-state heat balance equations under the dynamic load have been presented considering the viscosity-temperature relationship of the lubricant. Afterwards, the dynamic load analysis, the temperature analysis, the FHG analysis and the influence of the ambient temperature have been accomplished. Some new discovers are shown below:

(1) The dynamic load of the inter-shaft bearing is able to mirror the dynamic properties of the dual-rotor system. It is more proper for the dynamic load to depict the practical load of the inter-shaft bearing especially in the "resonance zone" of the system, rather than the static load commonly used in the previous literature.

(2) The dynamic behaviours of the dual-rotor system are coupled with the thermal behaviours of the inter-shaft bearing. In the "resonance zone" of the system, the temperature increases so sharply that two "temperature peak" are formed just like "resonance peak". In the "non-resonance zone" of the system, the temperature increases gradually.

(3) The total FHG shows the same behaviours with the inter-shaft bearing's temperatures. In the "resonance zone" of the system, the load FHG plays a leading role because the dynamic load increases rapidly here. In the "non-resonance zone" of the system, the viscosity FHG plays a leading role because the dynamic load is very small here.

(4) The ambient temperature has an opposite effect on the temperature and the total FHG. As the ambient temperature increase, the temperature-rotation speed curve moves upward, while the total FHG-rotation speed curve moves downward.

The future study will focus on the verification of the unsteady-state heat balance equations under the inter-shaft bearing's dynamic load by experiment.

Acknowledgements Thanks very much for the funding of the National Major Science and Technology Projects of China (No. 2017-IV-0008-0045), the National Natural Science Foundation of China (No. 11972129) and the Educational Department of Liaoning Province (No. LJGD2019009).

Declarations

Conflict of interest The authors declare that they have no conflict of interest.

References

1. Li QH, Hamilton JF (1985) Investigation of the transient response of a dual-rotor system with intershaft squeeze-film damper. J Eng Gas Turb Power 108(4):613–618
2. Aramaki H, Cheng HS, Zhu D (1992) Film thickness, friction, and scuffing failure of rib/roller end contacts in cylindrical roller bearings. J Tribol 114(2):311–316
3. Palmgren A, Ruley B (1945) Ball and roller bearing engineering. SKF Industries, inc., Philadelphia
4. Burton RA, Staph HE (1967) Thermally activated seizure of angular contact bearings. ASLE Trans 10:408–417
5. Sud ON, Davies PB, Halling J (1974) The thermal behaviour of rolling bearing assemblies subjected to preload. Wear 27:237–249
6. Harris TA, Kotzalas MN (2006) Essential concepts of bearing technology. Taylor & Francis, United Kingdom
7. Winer WO, Bair S, Gecim B (1986) Thermal resistance of a tapered roller bearing. ASLE Trans 29(4):539–547
8. DeMul JM, Vree JM, Maas DA (1989) Equilibrium and associated load distribution in ball and roller bearings loaded in five degrees of freedom while neglecting friction—Part I: general theory and application to ball bearings. J Tribol 111(1):149–155
9. DeMul JM, Vree JM, Maas DA (1989) Equilibrium and associated load distribution in ball and roller bearings loaded in five degrees of freedom while neglecting friction—Part II: Application to roller bearings and experimental verification. J Tribol. https://doi.org/10.1115/1.3261865
10. Jorgensen BR, Shin YC (1997) Dynamics of machine tool spindle/bearing systems under thermal growth. J Tribol 119(4):875–882

11. Stein JL, Tu JF (1994) A state-space model for monitoring thermally induced preload in anti-friction spindle bearings of high-speed machine tools. J Dyn Syst Meas Contr 116(3):372–386
12. Kim SM, Lee SK (2001) Prediction of thermo-elastic behavior in a spindle-bearing system considering bearing surroundings. Int J Mach Tool Manuf 41:809–831
13. Sun G, Palazzolo A, Provenza A, Lawrence C, Carney K (2008) Long duration blade loss simulations including thermal growths for dual-rotor gas turbine engine. J Sound Vib 316:147–163
14. Jiang SY, Mao HB (2011) Investigation of the high speed rolling bearing temperature rise with oil–air lubrication. J. Tribol 133:021101
15. Ma F, Li Z, Qiu S et al (2016) Transient thermal analysis of grease-lubricated spherical roller bearings. Tribol Int 93:115–123
16. Takabi J, Khonsari MM (2013) Experimental testing and thermal analysis of ball bearings. Tribol Int 60:93–103
17. Ai S, Wang W, Wang Y, Zhao Z (2015) Temperature rise of double-row tapered roller bearings analyzed with the thermal network method. Tribol Int 87:11–22
18. Than VT, Huang JH (2016) Nonlinear thermal effects on high-speed spindle bearings subjected to preload. Tribol Int 96:361–372
19. Gao S, Chatterton S, Naldi L, Pennacchi P (2021) Ball bearing skidding and over-skidding in large-scale angular contact ball bearings Nonlinear dynamic model with thermal effects and experimental results. Mech Sys Signal Process 147:107120
20. Hibner DH (1975) Dynamic response of viscous-damped multi-shaft jet engines. J Aircr 12(4):305–312
21. Gupta K, Gupta KD, Athre K (1993) Unbalance response of a dual rotor system: theory and experiment. J Vib Acoust 115(4):427–435
22. Ferraris G, Maisonneuve V, Lalanne M (1996) Prediction of the dynamic behavior of non-symmetric coaxial co- or counter-rotating rotors. J Sound Vib 154(4):649–666
23. Guskov M, Sinou JJ, Thouverez F, Naraikin OS (2007) Experimental and numerical investigation of a dual-shaft test rig with intershaft bearing. Int J Rotat Mach. https://doi.org/10.1155/2007/75762
24. Sun CZ, Chen YS, Hou L (2016) Steady-state response characteristics of a dual-rotor system induced by rub-impact. Nonlinear Dyn 86(1):91–105
25. Gao P, Hou L, Yang R, Chen YS (2019) Local defect modelling and nonlinear dynamic analysis for the inter-shaft bearing in a dual-rotor system. Appl Math Model 68:29–47
26. Gao P, Hou L, Chen YS (2019) Nonlinear vibration characteristics of a dual-rotor system with inter-shaft bearing. J Vib Shock 38(15):1–10
27. Tandon N, Choudhury A (1999) A review of vibration and acoustic measurement methods for the detection of defects in rolling element bearings. J Tribol 32(8):469–480
28. Hou L, Chen YS, Fu YQ, Chen HZ, Lu ZY, Liu ZS (2017) Application of the HB-AFT method to the primary resonance analysis of a dual-rotor system. Nonlinear Dyn 88(4):2531–2551
29. Okoya SS (2016) Flow, thermal criticality and transition of a reactive third-grade fluid in a pipe with Reynolds' model viscosity. J Hydrodyn 28(1):84–94
30. Holman JP (2010) Heat Transfer, 10th edn. McGraw Hill, New York, pp 51–52
31. Gao P, Chen YS, Hou L (2020) Nonlinear thermal behaviors of the inter-shaft bearing in a dual-rotor system subjected to the dynamic load. Nonlinear Dyn 101(1):191–209
32. Muzychka YS, Yovanovich MM (2001) Thermal resistance models for non-circular moving heat sources on a half space. J Heat Transfer 123(4):624–632
33. Fand RM (1965) Heat transfer by forced convection from a cylinder to water in crossflow. J Heat Mass Transfer 8(7):995–1010
34. Gazley C (1958) Heat-transfer characteristics of the rotational and axial flow between concentric cylinders. Trans ASME 108:79–90
35. Bjorklund IS, Kays WM (1959) Heat transfer between concentric rotating cylinders. J Heat Transfer 81(3):175–186
36. Yang ZL, Zhuo XR, Yang C, Song YZ (2002) An experimental research on convective heat transfer on the surface of horizontal cylinder rotating with high speed. Ind Heat 5:17–20

Publisher's Note Springer Nature remains neutral with regard to jurisdictional claims in published maps and institutional affiliations.